



HAL
open science

Can we improve the realism of gravity wave parameterizations by imposing sources at all altitudes in the atmosphere?

B Ribstein, C Millet, F Lott, A de La Cámara

► **To cite this version:**

B Ribstein, C Millet, F Lott, A de La Cámara. Can we improve the realism of gravity wave parameterizations by imposing sources at all altitudes in the atmosphere?. *Journal of Advances in Modeling Earth Systems*, 2021, 10.1029/2021MS002563 . hal-03366244

HAL Id: hal-03366244

<https://hal.science/hal-03366244>

Submitted on 5 Oct 2021

HAL is a multi-disciplinary open access archive for the deposit and dissemination of scientific research documents, whether they are published or not. The documents may come from teaching and research institutions in France or abroad, or from public or private research centers.

L'archive ouverte pluridisciplinaire **HAL**, est destinée au dépôt et à la diffusion de documents scientifiques de niveau recherche, publiés ou non, émanant des établissements d'enseignement et de recherche français ou étrangers, des laboratoires publics ou privés.

1 **Can we improve the realism of gravity wave**
2 **parameterizations by imposing sources at all altitudes**
3 **in the atmosphere?**

4 **B. Ribstein¹, C. Millet^{1,2}, F. Lott³, and A. de la Cámara⁴**

5 ¹CMLA, ENS Cachan, CNRS, Université Paris-Saclay, 94235 Cachan, France

6 ²CEA, DAM, DIF, F-91297 Arpajon, France

7 ³LMD, PSL Research Institute, Ecole Normale Supérieure, Paris, France

8 ⁴Dept. Earth Physics and Astrophysics, Universidad Complutense de Madrid (UCM), Spain

9 **Key Points:**

- 10 • Non-orographic gravity wave parameterization is improved by including inertial
11 waves and waves sources at all model levels.
- 12 • Parameterized energy spectrum becomes much closer to observations.
- 13 • Global model with the new parameterization performs well, some model biases are
14 modestly alleviated.

Corresponding author: Alvaro de la Cámara, acamarai@ucm.es

Abstract

A multiwave non-orographic gravity waves (GWs) scheme is adapted to represent waves of small intrinsic phase speed, inertial waves, and wave emission from all altitudes. This last change removes the launching altitude parameter, an arbitrary parameter systematically used in GW schemes. In offline calculations using reanalysis fields, these changes impose larger amplitude saturated waves everywhere in the middle atmosphere, which produces more realistic GW vertical spectra than in previous configurations. The same scheme, tested online in the Laboratoire de Météorologie Dynamique Zoom (LMDz) general circulation model, performs at least as well as the operational non-orographic GW scheme. Some modest benefits are seen, for instance, in the equatorial tilt with altitude of the winter jets in the middle atmosphere. Although the scheme includes the effects of inertial waves, which are detected in the mesosphere by different observational platforms, the configuration that gives a reasonable climatology in LMDz hinders their vertical propagation and limits their presence at mesospheric altitudes.

Plain Language Summary

Gravity waves are fluctuations in the atmosphere (seen in the temperature, wind velocity, and pressure fields) that transport energy and momentum from their sources in the troposphere and middle atmosphere to their sinks in the middle atmosphere. This way they exert a profound influence on the global circulation. Due to their relative small spatial scales, atmospheric general circulation models do not explicitly resolve these waves, and their effects on the circulation resolved by the model need to be parameterized. Parameterizations of gravity waves generated by fronts and flow imbalances typically assume that wave sources are at a certain vertical level in the troposphere, which is easy to implement but neglects the fact that these processes can occur at all altitudes in the atmosphere. In this study, we explore to which extent parameterizations of gravity wave due to fronts and flow imbalances can be improved by allowing waves to be emitted from all model levels. Our results show evidence of modest corrections of some model biases, and a clear improvement in the parameterized gravity waves energy spectra.

1 Introduction

Atmospheric gravity waves (GWs) have long been observed with radio soundings (Tsuda et al., 1994), using radars (Love & Murphy, 2016; Shibuya & Sato, 2019), lidars (Baumgarten

46 et al., 2016; Khaykin et al., 2015), and satellites (Alexander, 2015). Their amplitude grows
47 as they propagate vertically and they impact the middle atmosphere circulation when
48 they break, even if they have relatively small amplitudes at the source level. The spa-
49 tial scales of GWs are generally too small to be resolved by general circulation models
50 (GCMs), and the generation, propagation and dissipation of these waves need to be pa-
51 rameterized for GCMs to produce a reasonable circulation. Such parameterizations were
52 first introduced in the 1980’s in models with a barely resolved stratosphere, and only high-
53 amplitude orographically-forced GWs were needed to be taken into account (Palmer et
54 al., 1986). Nowadays, most models resolve the middle atmosphere requiring the param-
55 eterization of the effects of smaller-amplitude, non-orographic gravity waves (Manzini
56 et al., 1997).

57 One way to parameterize non-orographic GWs consists in using the observational
58 evidence that over a large number of realizations the GW fluctuations of vertical wind
59 and temperature in the middle atmosphere follow a “universal” spectra, which shape is
60 derived from radiosondes and satellite data (e.g., Cot, 2001; Zhao et al., 2017). These
61 spectra are numerically robust (Lindborg, 2006; Brethouwer et al., 2007), and various
62 theories have been developed to explain them. Some involve wave breaking (e.g., Dewan
63 & Good, 1986), whereas other include nonlinear effects like triade interactions, Doppler
64 spreading, and inverse cascades (e.g., Broutman & Young, 1986; Lilly, 1983; C. Hines,
65 1996; Métais et al., 1996). Beyond the theoretical debate, a practical result is that the
66 existence of a saturated spectra allows semi-theoretical integrations that ease the param-
67 eterization of non-orographic GWs (C. O. Hines, 1997; Warner & McIntyre, 1996; Manzini
68 et al., 1997). To a certain extent, this approach is challenged by the recent balloon ob-
69 servations showing that the GW field is very intermittent, and is often dominated by rather
70 well-defined GWs packets (Hertzog et al., 2008; Wright et al., 2013; Alexander, 2015).
71 This intermittent nature makes that in each model gridbox and at each time step, the
72 number of GWs packets is not large enough to fulfill the law of large numbers underly-
73 ing the construction of spectra out of individual realisations. More generally, this con-
74 cern is related to that of statistical equilibrium and is central in the recent development
75 of stochastic parameterizations (Berner et al., 2017). In the case of the GWs this im-
76 plies that the “universal” spectral shape should be checked a posteriori and over a large
77 number of days, rather than being realised every time. This leads to an alternative ap-
78 proach to parameterize non-orographic GWs, which is based on representing the GW

79 field with a Fourier series in the horizontal and temporal directions (e.g., Alexander &
 80 Dunkerton, 1999). In this approach the individual harmonics are a crude representation
 81 of the individual wave packets and the intermittency is taken into account by launch-
 82 ing stochastically a few harmonics each timestep (Eckermann, 2011; Lott, Guez, & Maury,
 83 2012). The challenge is then to reconcile the two types of schemes (“spectral” versus “mul-
 84 tiwave”) and the two types of observations (stationary universal “vertical spectra” ver-
 85 sus intermittent “wave packets”). As we shall see, this can be done by showing that the
 86 ensemble average of the periodograms associated with superposed harmonics can repro-
 87 duce the observational “universal” spectra (de la Cámara et al., 2014). In route to re-
 88 alize this objective, the study of (Souprayen et al., 2001) is encouraging since it shows
 89 that the wave filtering by the large scale flow and the breaking of individual GWs pack-
 90 ets can yield realistic spectra in the upper stratosphere and mesosphere.

91 In some modeling centers the amplitude of the parameterized GWs is related to
 92 their non-orographic sources, i.e. convection and fronts and/or flow imbalance, and the
 93 GWs are launched from a single source level in the troposphere. This last choice is not
 94 well justified for several reasons. One is that the presence of unbalanced flows that emit
 95 GWs is not restricted to the troposphere: Dörnbrack et al. (2018) and Sato and Yoshiki
 96 (2008) provide observational evidence for GW generation in the stratospheric polar vor-
 97 tex, and Polichtchouk and Scott (2020) discuss the generation from the critical layer of
 98 the stratospheric polar night jet using an idealized numerical model. A second reason
 99 is that observations often show that the GWs in the middle atmosphere have rather long
 100 periods (often around 6 hours and longer in Reichert et al. (2019), near the inertial pe-
 101 riod in Gelinias et al. (2012), Bellenger et al. (2017), Shibuya and Sato (2019), and Vincent
 102 and Alexander (2020)). The presence of these slow waves is difficult to justify if the GW
 103 sources are only in the troposphere, as waves with small intrinsic frequency have short
 104 vertical wavelengths and saturate more easily than faster waves. This process is often
 105 referred to as dynamical filtering and occurs systematically when the waves approach
 106 a critical level. For GWs, this dynamical filtering is very effective, explaining most of the
 107 relation between the wind speed and GW amplitude in balloon measurements (Plougonven
 108 et al., 2017).

109 The present paper analyses if the “multiwave” non-orographic GW parameteriza-
 110 tion due to fronts and jets of de la Cámara and Lott (2015) can be adapted to include
 111 sources from all levels, small intrinsic phase speed waves (including near inertial waves),

112 and if these modifications can help to reproduce the universal spectral shape systemat-
113 ically enforced in the “spectral schemes”. Although some of these concerns could be addressed
114 with any other scheme, this one has few characteristics that makes it suitable to treat
115 all of them. The first and most important is that this scheme is based on a spontaneous
116 emission theory (Lott, Plougonven, & Vanneste, 2012), which is a theory that partly ex-
117 plains the GW emission seen in quite sophisticated high resolution simulations (Polichtchouk
118 & Scott, 2020), and which is not limited to the troposphere. The second is that it points
119 to PV anomalies as a source of GWs, which is coherent with the fact that processes such
120 as “classical” geostrophic adjustment or re-emission are associated with the presence
121 of PV anomalies. The third is that it is operational in the Institute Pierre Simon Laplace
122 (IPSL) Earth system model (Hourdin et al., 2013), so it is routinely tested. The fourth
123 is about observational constraints, in the sense that it qualitatively produces the observed
124 intermittency of the nonorographic GW field (Hertzog et al., 2012; Wright et al., 2013;
125 de la Cámara et al., 2014; Alexander, 2015). Indeed, de la Cámara, Lott, Jewtoukoff,
126 et al. (2016) demonstrated that a good representation of the GW intermittency can be
127 beneficial for models, helping the IPSL model to better simulate the timing of the South-
128 ern Hemisphere stratospheric final warming. A final (and much less positive) reason is
129 that in its operational version, de la Cámara and Lott (2015) use a Gaussian distribu-
130 tion of intrinsic phase speeds with standard deviation near 40ms^{-1} . This large value is
131 used because it helps the waves to propagate up to the upper mesosphere without at-
132 tenuation, but it contradicts the fact that frontal waves resulting from spontaneous ad-
133 justment have small intrinsic phase speeds near their source (Lott, Plougonven, & Vanneste,
134 2012).

135 A central assumption made in this paper is that this bias toward larger than ex-
136 pected intrinsic phase speeds is common to other schemes, and that trying to correct it
137 in one scheme could be indicative of what could be done in other schemes. In fact the
138 corrections we test in this study have a general character: we include the Coriolis force
139 because it can be significant at low intrinsic frequencies, and we place sources at all lev-
140 els rather than in the troposphere only. Finally, it is worth noting that the shortcom-
141 ings we try to deal with are today considered as priorities in the community (see discus-
142 sion about low phase speed waves in Alexander et al. (2021)), but are not the only ones.
143 Some authors place more emphasis on including three-dimensional propagation of grav-
144 ity waves in parameterizations (e.g., Muraschko et al., 2015; Ribstein & Achatz, 2016;

145 Amemiya & Sato, 2016). Including lateral propagation in highly parallelized code is ex-
 146 tremely challenging computationally, so it is worthwhile to test if some improvements
 147 can be obtained through other routes.

148 The goal of this paper is to present modifications so that the frontal GWs param-
 149 eterization can include slow intrinsic phase speed waves, rotation and GWs sources at
 150 all levels in the atmosphere. Section 2 describes the modifications we propose to the frontal
 151 GWs parameterization used in LMDz. In section 3, offline tests are performed to test
 152 if the scheme predicts realistic vertical energy spectra. Section 4 presents online results
 153 obtained with the LMDz GCM, using the standard parameterization and the updates.
 154 Section 5 gives the main conclusions.

155 2 Non-orographic gravity waves due to fronts and flow imbalance

156 2.1 General formalism

157 We next summarize the formalism of the stochastic parameterization used in LMDz
 158 (de la Cámara & Lott, 2015), and emphasize the modifications introduced in this study.
 159 The horizontal wind and temperature disturbances (\mathbf{u}', T') due to GWs are represented
 160 by a stochastic Fourier series of J monochromatic waves,

$$(\mathbf{u}', T')(\mathbf{x}, z, t) = \sum_{j=1}^J C_j \left(\hat{\mathbf{u}}_j(z), \hat{T}_j(z) \right) e^{i(\mathbf{k}_j \cdot b f x - \omega_j t)} \quad (1)$$

161 whose horizontal wavevector \mathbf{k}_j and absolute frequency ω_j are chosen randomly, and the
 162 complex amplitudes $\left(\hat{\mathbf{u}}_j(z), \hat{T}_j(z) \right)$ vary in the vertical direction measured by the log-
 163 pressure coordinate z . The intermittency coefficient C_j measures the probability of the
 164 presence of the corresponding wave at a given horizontal location within the gridbox. In
 165 previous versions of the parameterization we had always assumed equiprobability for sim-
 166 plicity and taken

$$\sum_{j=1}^J C_j^2 = 1, \text{ i.e. } C_j = 1/\sqrt{J}. \quad (2)$$

167 As we shall see, the value of this parameter can be changed as to represent sources lo-
 168 cated at different vertical levels.

169 To evaluate the wave amplitude, we adapt Lott, Plougonven, and Vanneste (2012)'s
 170 analytical estimate of the GW momentum flux emitted by a potential vorticity (PV) anomaly
 171 in a vertically sheared flow, and consider that a given model level z_i of thickness dz_i emits

172 a vertical Eliassen-Palm (EP) flux with value,

$$\mathcal{F}(z_l) = G_0 \frac{\Delta z dz_l}{4f_0} \rho(z_l) N(z_l) \left[f \tanh \left(\frac{\zeta(z_l)}{f} \right) \right]^2 e^{-\pi \frac{N(z_l)}{U_z(z_l)}}, \quad (3)$$

173 where $U_z = |\mathbf{U}_z|$ is the modulus of the vertical shear, N is the Brunt-Väisälä frequency,
 174 $\rho = e^{-z/H}$, and $H = 7\text{km}$ is the characteristic vertical scale of density decay. Still in
 175 equation (3), G_0 is a tuning parameter, $f_0 = 10^{-4}\text{s}^{-1}$ is a characteristic value of f , Δz
 176 a characteristic depth of the subgrid scale PV anomalies. To derive equation (3) from
 177 theory we made the approximation that the subgrid scale vorticity equals the gridscale
 178 one ζ . The only novelty at this stage is the hyperbolic tangent term that is used to limit
 179 the relative vorticity to values below $|f|$. This is a reasonable assumption since flows with
 180 relative vorticity larger than $|f|$ are likely to be strongly unstable, and it also moderates
 181 the emission intensity in the tropics.

182 de la Cámara and Lott (2015) assumed that the momentum fluxes essentially come
 183 from the troposphere, but integrated the contributions in equation (3) over all model lev-
 184 els L , to calculate a total emitted flux,

$$F = \sum_{l=1}^L \mathcal{F}(z_l). \quad (4)$$

185 It is then imposed that this momentum radiates from a specified launching level z_{La} in
 186 the troposphere, distributed over the ensemble of J monochromatic waves in (1). Among
 187 the randomly chosen parameters, the direction of each harmonic \mathbf{F}_j of the total EP-flux
 188 F is specified through the random horizontal wvector \mathbf{k}_j , following the rule

$$\mathbf{F}_j(z_{La}) = -\frac{\mathbf{k}_j}{\|\mathbf{k}_j\|} F. \quad (5)$$

189 To derive (5) from (4) we have chosen by convention that the sign of the intrinsic phase
 190 speed at the launch level

$$\hat{\omega}_j(z_{La}) = \omega_j - \mathbf{k}_j \cdot \mathbf{U}(\mathbf{z}_{La}) > 0. \quad (6)$$

191

192 To evaluate the vertical profile of the flux above the launching level we consider
 193 that from one vertical level to the next above, the flux is (i) reduced by a small diffu-
 194 sivity $\mu/\rho_0(z)$, (ii) limited by that of a saturated wave (e.g., Lindzen & Schoeberl, 1982),
 195 and (iii) set to zero immediately above an inertial level (Lott et al., 2015):

$$\mathbf{F}_j(z_{l+1}) = -\frac{\mathbf{k}_j}{\|\mathbf{k}_j\|} \Theta \left(\hat{\omega}_j(z_{l+1})^2 - f^2 \right) \times$$

196

$$\min \left\{ \|\mathbf{F}_j(z_l)\| \exp \left(2 \frac{\mu m_j^3(z_l)}{\rho_0 \hat{\omega}_j(z_l)} dz_l \right), \rho_r S_c^2 \frac{N(z_{l+1})^2}{|m_j(z_{l+1})|^3} \frac{k_{\min}^2}{\|\mathbf{k}_j\|} \right\}. \quad (7)$$

197

198

199

200

201

In equation (7), Θ is the Heaviside function to handle inertial levels, k_{\min} is the horizontal wave number associated with the largest resolved GW in the model (it is related to the model's horizontal resolution), and S_c is a tunable parameter that controls the saturation amplitude. Still in equation (7), the vertical wavenumber m_j and intrinsic frequency $\hat{\omega}_j$ are given by

$$m_j(z) = -\frac{N(z)\|\mathbf{k}_j\|}{\sqrt{\hat{\omega}_j(z)^2 - f^2}}, \text{ where } \hat{\omega}_j(z) = \omega_j - \mathbf{k}_j \cdot \mathbf{U}(z), \quad (8)$$

202

203

where the minus sign in the definition of m_j ensures upward propagation above the launching level. A novelty is that we have included the Coriolis force in equations (7) and (8).

204

205

206

207

208

209

210

211

212

213

214

215

216

217

218

219

At this stage, the emitted flux is equidistributed among all possible horizontal directions, which somehow contradicts the theory saying that the preferential emission is in the direction opposite to the wind shear. In practice, however, waves emitted with phase speeds in the direction of the shear get their intrinsic phase speeds decreased and their vertical wave numbers increased as they are evaluated at the next vertical level above. According to (7) the fluxes for these waves are much more reduced than for the waves in the direction opposed to it. In the scheme we also do exclude the emission of highly saturated waves, which also avoid imposing a huge drag just above the launching level, by systematically replacing the launching value of the flux by its value at the level above (in $z_{La+1} = z_{La} + dz_{La}$). This naturally tends to reduce emissions of waves with phase speeds in the direction of the shear. Finally, below the launching altitude the fluxes are kept constant, which technically allows to define $\mathbf{F}_j(z)$ at all model levels. This last choice is consistent with the fact that in the model we do not extract momentum from the source's surroundings region to balance the emitted wave drag, a shortcoming that is justified by the rapid decrease of air density with altitude: the corrections to the fields and to the tendencies would presumably be of small amplitude around and below the launch level.

220

221

Once $\mathbf{F}_j(z)$ is evaluated at all vertical levels, we use the Wentzel-Kramers-Brillouin (WKB) formalism to relate the EP flux to the disturbance fields in (1):

$$\hat{\mathbf{u}}_j(z) = \frac{-\mathbf{k}_j \hat{\omega}_j - if \mathbf{e}_z \times \mathbf{k}_j}{\hat{\omega}_j^2 - f^2} \phi_j(z) e^{i \int_0^z m_j(z') dz' + i \xi_j}, \quad (9)$$

222

$$\hat{\mathbf{T}}_j(z) = im_j \frac{H}{R} \phi_j(z) e^{i \int_0^z m_j(z') dz' + i \xi_j} \quad (10)$$

223 where the amplitude of the geopotential is

$$\phi_j(z) = \sqrt{\frac{\|\mathcal{F}_j\|N}{\rho m_j \|\mathbf{k}_j\|}}, \quad (11)$$

224 and ξ_j is a phase with no effect on the EP fluxes, which is chosen randomly when com-
 225 puting the physical fields offline. For completeness, note that the GW drag is computed
 226 as

$$\frac{\partial \mathbf{u}}{\partial t}|_{\text{GW}} = \sum_{j=1}^J C_j^2 \frac{\partial \mathbf{F}_j}{\partial z}. \quad (12)$$

227 Thermal effects are taken into account by evaluating the work performed against the wind:

$$\frac{\partial T}{\partial t}|_{\text{GW}} = -\mathbf{u} \cdot \frac{\partial \mathbf{u}}{\partial t}|_{\text{GW}}/C_p, \quad (13)$$

228 where C_p is the heat capacity of dry air.

229 At this point, we have applied the described equations to J waves emitted at a sin-
 230 gle launching level, z_{La} . To adapt our formalism in order to work with J waves emit-
 231 ted from different launching levels we choose the launching level randomly, z_j , together
 232 with the horizontal wavevector \mathbf{k}_j and intrinsic frequency $\hat{\omega}_j$ (see Fig. 1). Then the launch-
 233 ing flux in (5) is replaced by

$$\mathbf{F}_j(z_j) = -\frac{\mathbf{k}_j}{\|\mathbf{k}_j\|} \mathcal{F}(z_j), \quad (14)$$

234 the emitted amplitude \mathcal{F} at the corresponding level being directly given by (3). The var-
 235 ious profiles are then evaluated above and below z_j following equations (7) to (11), but
 236 with z_{La} replaced by z_j for each waves. But now that we have J different launching al-
 237 titudes, with the possibility that $J \neq L$, we need to take for intermittency parameter:

$$C_j^2 = L/J. \quad (15)$$

238 **2.2 Model and reanalysis**

239 In offline mode we use daily fields of temperature and horizontal winds from the
 240 Modern-ERA Retrospective Analysis for Research and Applications version 2 (MERRA2)
 241 (Gelaro et al., 2017) at $1^\circ \times 1^\circ$ resolution and from the ground to 0.01hPa.

242 In online mode we use the stratospheric version of the Laboratoire de Meteorolo-
 243 gie Dynamique Zoom (LMDz) model with 142×144 uniform latitude longitude grid and
 244 $L = 80$ vertical levels, the model top being at 0.01hPa. The simulations are forced with
 245 the observed seasonal cycle of sea surface temperatures and sea-ice from the CMIP5 database
 246 for the period 1980-1995, and the ozone climatology is built from the ACC/SPARC ozone

247 database. All runs have the same settings of the orographic and convective GWs param-
 248 eterizations (Lott & Miller, 1997; Lott & Guez, 2013), the different setting of the param-
 249 eterization of the GWs due to fronts and jet imbalances are detailed in the next subsec-
 250 tion. The reader is referred to Hourdin et al. (2020) for a comprehensive description of
 251 the LMDz model equations and specifications of its grid.

252 2.3 Gravity waves parameterization setup

253 In all experiments discussed in this paper, we consider $J = 48$ waves each phys-
 254 ical time step in the model as well as in the offline reconstructions. We also choose the
 255 horizontal wavenumber amplitude $k_j = \|\mathbf{k}_j\|$ with uniform probability in the interval
 256 $k_{\min} \leq k_j \leq k_{\max}$, with $2\pi/k_{\max} = 6.3\text{km}$ and $2\pi/k_{\min} = 315\text{km}$ crudely bounding
 257 the smallest horizontal wavelengths that can be attributed to GWs, and the largest hor-
 258 izontal wavelength that cannot be represented in the model gridbox. The direction of
 259 horizontal propagation θ_j ($\mathbf{k}_j = k_j(\cos\theta_j\mathbf{i} + \sin\theta_j\mathbf{j})$) is chosen uniformly within the
 260 interval $0 \leq \theta_j \leq 2\pi$. The attribution of frequency is indirect since we first select the
 261 wave intrinsic phase speed at the launch level z_l from a half-normal distribution with a
 262 standard deviation of c_φ , and in the direction given by \mathbf{k}_j . The parameter c_φ is key, and
 263 tuning it in different experimental setups requires adjustments in the launched momen-
 264 tum flux amplitude and saturation parameters G_0 and S_c in (3) and (7) respectively.

265 In this study we present results from three different setups of the nonorographic
 266 GWs parameterizations. The strategy adopted consists of (1) decreasing the phase speed
 267 drastically and (2) introduce multiple level sources adapting the other parameters to give
 268 performances that are quite comparable to the existing operational scheme. We there-
 269 fore target rather neutral effects on the model climate, which is in itself a task that de-
 270 mands a substantial amount of trial simulations.

271 In the first experimental setup, we proceed as in de la Cámara and Lott (2015) and
 272 choose the launching altitude at $z_{La} = 500$ m, and take $c_\varphi = 50 \text{ m}\cdot\text{s}^{-1}$, $G = 4$, and
 273 $S_c = 0.6$. These values stay reasonably close to those used in previous studies (e.g., de
 274 la Cámara, Lott, & Abalos, 2016) considering that we now include the Coriolis force and
 275 bound the disturbance vorticity to values below f . If we consider that the characteris-
 276 tic vertical scale of the waves produced with this setup is $2\pi/m \approx 2\pi c_\varphi/N \approx 20\text{km}$,

277 we see that we are essentially taking into account long waves (since c_φ is large), and we
 278 will refer to this setup as LW.

279 In the second experimental setup we keep a single launching level but decreases the
 280 intrinsic phase speed down to $c_\varphi = 10\text{ms}^{-1}$. This requires a slight increase in G up to
 281 $G = 5$, but since the characteristic vertical scale is now much shorter, i.e. $2\pi c_\varphi/N \approx$
 282 4km, the saturation parameters need to be increased substantially up to $S_c = 2.5$ to
 283 keep the saturated flux of about the same amplitude within the middle atmosphere. Note
 284 that the characteristic vertical scale is closer to the wavenumber m^* introduced by Warner
 285 and McIntyre (1996). These changes in the wave parameters imply parameterized waves
 286 of shorter vertical scales, so this setup will be referred to as SW-1L.

287 In the third experimental setup, we consider waves emitted from multiple model
 288 levels. Nevertheless we realized that as the amplitude of emission in equation (3) is very
 289 sensitive to the Richardson number and to the relative vorticity ζ , there is often one level
 290 that dominates the sum of EP fluxes in equation (5). Finding this level out of J cases
 291 is equivalent to average over J levels, so there is no need to change substantially the tun-
 292 ing parameters G and S_c compared to the previous case, and we take for the new val-
 293 ues $G = 4.2$ and $S_C = 3$. This configuration will be referred to as SW-ML.

294 **3 Parameterized gravity wave spectra**

295 The performance of the three configurations LW, SW-1L, and SW-ML is addressed
 296 in off-line runs using the meteorological fields from MERRA2 as input. Figures 2a-b show
 297 the spatial distribution on a given day (22 January 2012) of the daily average of verti-
 298 cal EP flux amplitude in SW-ML at the 500 hPa level. Peak values of around 50 mPa
 299 are found in the vicinity of the subtropical jets in both hemispheres, reflecting the di-
 300 rect relation between the emitted EP flux and the grid-scale relative vorticity, as indi-
 301 cated by equation (3). Figure 2c compares the latitudinal distribution of the zonal-mean
 302 EP flux for LW, SW-1L, and SW-ML. The three curves present very similar features with
 303 very low values in the tropics, a maximum around the subtropical jets, and a gradual
 304 descent towards the poles. In general, we see that SW-ML represents slightly larger fluxes
 305 at all latitudes than the other two setups, and that SW-1L consistently works with smaller
 306 fluxes. It is important to emphasize that although the amplitude of the EP flux is cal-
 307 culated deterministically, the probability density function of the launched fluxes qual-

308 itatively follows the observed log-normal distribution in the lower stratosphere (not shown
 309 but see de la Cámara and Lott (2015)).

310 Next we analyze the ability of LW, SW-1L and SW-ML to reproduce the empir-
 311 ical GW energy spectra. The vertical profiles of the wind and temperature are obtained
 312 from the parameterized profile of vertical EP flux as in equations (9), (10), and (11). More
 313 specifically, and to build spectra out of individual realisations we first construct 1000 monochro-
 314 matic waves, each corresponding to randomly chosen values of phase speed and horizon-
 315 tal wavenumber. The wind and Temperature profiles of each wave are then sampled ev-
 316 ery 100m, which is a much higher vertical resolution than that used in MERRA2. We
 317 therefore linearly interpolate the EP flux to the target grid, together with the large scale
 318 fields of wind and Temperature needed in Eqs (9) and (10). To construct 1 realization
 319 out of these 1000 monochromatic waves, we pick $J = 48$ of them randomly, choose the
 320 phase ξ_i of each randomly and then sum over the J waves. Let $u'(z)$ be one such real-
 321 ization of the horizontal wind disturbance, we use here the same notation as in (1), we
 322 then perform a Fourier analysis of this realisation which gives the periodogram $\hat{\mathbf{u}}\hat{\mathbf{u}}^*$, \hat{u}
 323 being the Fourier coefficients and the stars indicating conjugation. To avoid numerical
 324 artifacts in the boundaries, a tapered cosine window is used together before the fast Fourier
 325 transform. The spectra are then estimated at each horizontal places by doing an ensem-
 326 ble average of individual periodograms $\langle \hat{\mathbf{u}}\hat{\mathbf{u}}^* \rangle$ constructing an ensemble of 20 indepen-
 327 dent realisations. Although we found our results about spectral shape to be little sen-
 328 sitive to the procedure, we could have averaged at a given place over different days, or
 329 average the same day at different places, we adopt this one because it permits to com-
 330 pare without ambiguity regions with presumably large GW emission to regions with small
 331 GW emission (for instance the locations A and B in Figures 2a-b and the same day).

332 In the following we restrict the discussion to the horizontal wind spectra, but we
 333 verified that the temperature spectra exhibit a similar shape (not shown). The spectra
 334 for altitudes lower than 25 km and 65 km are displayed in Figure 3 at the two specific
 335 locations A and B and still for the 22 january 2012. For both locations the energy spec-
 336 tra obtained with the configurations LW and SW-1L are proportional to $m^{-4.5}$, the shape
 337 obtained with vertically distributed GW sources (i.e. SW-ML) is characterized by a m^{-3}
 338 tail, which is suggestive that saturation occurs much more systematically under this con-
 339 figuration (e.g., Dewan & Good, 1986). Besides, the vertical spectra for SW-1L and SW-

340 ML are shifted toward smaller wavelengths, which is consistent with the fact that GWs
 341 are launched with slower phase velocities.

342 To summarize, when smaller intrinsic phase speed are imposed (i.e. in SW-1L and
 343 SW-ML), there is more energy concentrated at shorter wavelengths, this energy corre-
 344 sponds more often to saturated waves, and the effect of the saturation on decreasing the
 345 wave amplitude is compensated in SW-ML by launching waves from all altitudes. These
 346 results demonstrate that multiwave schemes with small intrinsic phase speed can fairly
 347 reproduce the observed GW energy spectra, bridging a gap with the spectral schemes
 348 that include sources but prescribe a saturated spectrum (Bushell et al., 2015).

349 **4 Impacts on the simulation of the stratosphere**

350 We next evaluate the performance of the three configurations of the frontal GW
 351 parameterization in 15-year runs with the climate model LMDz. Figures 4a-b show latitude-
 352 height cross-sections of zonal-mean zonal wind in LW-LMDz (black contours), season-
 353 ally averaged for December-January-February (DJF) and June-July-August (JJA). Well-
 354 known features of the zonal mean structure of the troposphere and middle atmosphere
 355 are captured in LW-LMDz. The subtropical jets in the upper troposphere are stronger
 356 in the winter than in the summer hemisphere, and displaced further poleward in the sum-
 357 mer hemisphere. In the middle atmosphere, there are westerly winds in winter (i.e., the
 358 polar night jet) and easterlies in summer. The color shading in Figures 4a-b represents
 359 the difference of zonal wind between MERRA2 (period 1996-2010) and LW-LMDz. In
 360 the tropics, there are differences above 40-km height in all seasons that are related to
 361 the representation of the amplitude of the semiannual oscillation (Lott & Guez, 2013;
 362 Smith et al., 2017). In the extratropics, the strongest bias takes place in the upper strato-
 363 sphere and mesosphere in JJA in the SH (Figure 4b), where the weaker winds in LW-
 364 LMDz than in MERRA2 are related to a polar night jet in the model that does not tilt
 365 equatorward with height as compared to reanalysis. In the NH in DJF (Figure 4a), the
 366 westerly winds in LW-LMDz are also systematically weaker than in MERRA2, which im-
 367 plies a weaker polar vortex.

368 The middle and bottom panels of Figure 4 show the corresponding zonal wind pro-
 369 files (black contours) for SW-1L-LMDz (Figures 4c-d) and SW-ML-LMDz (Figures 4e-
 370 f), with the color shading displaying differences with respect to LW-LMDz. Both SW-

371 1L-LMDz and SW-ML-LMDz produce a stronger westerly jet in DJF in the upper strato-
 372 sphere and mesosphere than LW-LMDz, something consistent with MERRA2. In gen-
 373 eral, the differences between SW-1L-LMDz and LW-LMDz do not necessarily imply re-
 374 duced biases (cf. Figures 4a-b), but SW-ML-LMDz performs qualitatively better. This
 375 is particularly evident in the case of the polar night jet in the SH in JJA (Figure 4f), which
 376 tilts towards the tropics with altitude and the wind differences with LW-LMDz are sim-
 377 ilar to those between MERRA2 and LW-LMDz (Figure 4b).

378 To test if these changes can be associated with changes in GW drag, Fig. 5 shows
 379 the cross-sections of zonal mean non-orographic GW drag in SW-1L-LMDz and SW-ML-
 380 LMDz (black contours), and the corresponding differences with respect to the control
 381 run LW-LMDz (shading). The non-orographic GW drag is more effective at higher al-
 382 titudes in the upper stratosphere and mesosphere, where we find positive drag in the sum-
 383 mer hemisphere and negative drag in the winter hemisphere, contributing to decelerate
 384 the easterlies and westerlies, respectively. For SW-1L and SW-ML the differences of GW
 385 drag and zonal mean zonal wind with respect to LW are generally consistent with this
 386 view since regions of slower (larger) mesospheric winds roughly correspond to regions of
 387 smaller (larger) GW drag in Figure 5 (see the summer mesosphere between $60\text{km} < z <$
 388 80km and $80^\circ\text{S}-60^\circ\text{S}$ in Figs. 4c and 5c). As we have modified the phase speeds substan-
 389 tially, this correspondence between GW drag and zonal wind differences could be sim-
 390 ply related to changes in dynamical filtering at high altitude. In the regions mentioned
 391 before, this does not seem to be the case: weaker winds in summer should allow the prop-
 392 agation of more waves with positive intrinsic phase speeds that would strengthen the net
 393 positive drag, which is not what is found in summer in the upper mesosphere. There-
 394 fore, it would seem that the new sets of parameters are simply producing less GW drag
 395 and acceleration.

396 Dynamical filtering is more evident in the differences between the SW-ML run and
 397 the LW run and at the places where the differences in zonal wind are the more pronounced
 398 -i.e. at altitudes between 60km and 80km and around 30° in each hemisphere (Figures. 4(e)-
 399 (f)). The difference in GW drag at those places (Figures. 5(e)-(f)) shows a weaker drag
 400 in SW-ML below the jet shear zone, and a stronger drag above. The difference in sign
 401 between the two sides of the shear zone is essential, it reveals that we do not put glob-
 402 ally more or less drag, as was the case in summer for SW-1L, but that we distribute it
 403 differently according to the wind speed. Another important thing to notice is that the

404 latitudes around 30° also correspond to the latitudes of the winter tropospheric jet cen-
 405 ter at $z \approx 15\text{km}$. We can therefore speculate that since the wind shear is negative on
 406 the upper flank of the jet, positive phase speed waves are produced, they create accel-
 407 eration right above at mesospheric levels, but are not much efficient further above be-
 408 cause they have small intrinsic phase speeds and are easily filtered out by the wind they
 409 produces. Our explanation is therefore that the stratospheric jet tilt in the SH, which
 410 is reproduced in SW-ML-LMDz, is in part supported by GWs with small intrinsic phase
 411 speeds coming from the upper troposphere and lower stratosphere. This can be realized
 412 by a GW scheme with sources that are not confined to the troposphere.

413 Overall, the mean middle atmospheric circulation with the two new settings of the
 414 frontal GW parameterization (i.e. SW-1L and SW-ML) is reasonable, and presents spe-
 415 cific improvements in the shape of the austral winter jet that look promising to correct
 416 long-standing biases. To gain further confidence into the performances of the model in
 417 these new settings, we next evaluate the interannual variability of the different model
 418 runs. Figure 6 shows the annual cycle of the zonal mean temperature at 80°N and the
 419 variability over the period 1996-2010 quantified through the 5th and 95th percentiles (shad-
 420 ing). Starting with the control run LW-LMDz (red line and shading in Figure 6a), the
 421 model has a clear warm bias at 10 hPa as compared to MERRA2 (black line and shad-
 422 ing in Figure 6a, and Fig. 6d), which is consistent with a weak wind bias (Figure 4a).
 423 This temperature bias is reduced using the alternative settings SW-1L and SW-ML (Fig-
 424 ures 6b-c), both in the mean cycle and the variability given by the percentiles. However,
 425 the three model simulations clearly overestimate temperature fluctuations in early and
 426 late winter.

427 **5 Conclusions**

428 Specifying the emission of GWs based on the model grid-scale dynamics, and us-
 429 ing our observational knowledge of the GW field to constrain tunable parameters in the
 430 process, are two major challenges for improving parameterizations of GW drag (Alexander
 431 et al., 2010; Plougonven et al., 2020), particularly for GWs generated by fronts and jet
 432 imbalance (Plougonven & Zhang, 2014). The parameterization introduced in de la Cámara
 433 and Lott (2015) was based on a formalism that can be used to address these challenges.
 434 For this purpose we introduce the following modifications to this parameterization: 1)
 435 we reduce the horizontal intrinsic phase speeds of the launched waves following sugges-

436 tions from observations and high-resolution model runs (Plougonven et al., 2017) (SW-
437 1L configuration); and 2) we launch GWs from all model levels (SW-ML configuration)
438 instead of launching from only one tropospheric level. This can result in more saturated
439 waves everywhere in the middle atmosphere.

440 A technical result of our study is that launching GWs at different model levels can
441 be achieved at a moderate numerical cost, in our case the cost of the stochastic param-
442 eterization of non-orographic GWs used in LMDz. From a more scientific point of view,
443 some results are worth highlighting. The first is that decreasing the intrinsic phase speeds
444 and launching GWs from all levels shifts the slope of the vertical energy spectra of parametrized
445 GWs toward the observed value of -3 . Second, the middle atmospheric circulation in
446 climate model simulations responds reasonably well to the applied changes. There are
447 even some indications of a weak reduction of model biases, such as an improved equa-
448 torward tilt of the austral polar night jet and stratospheric polar temperatures over the
449 Arctic. These bias reductions may be model dependent, or could have been obtained in
450 the same model with further refined tuning of the initial scheme. However, we obtain
451 these results using configurations with about the same amount of wave stress launched
452 (see Figure 2c) and only moderate alterations of the parameters of the scheme. This may
453 indicate that the improvements obtained are not simply a signature of refined tuning.

454 Despite the modifications performed to the GW parameterization, placing inertial
455 gravity waves in the middle atmosphere suggested by observations (Gelinas et al., 2012)
456 has proven difficult (not shown). This may call for substantial changes in the formalism,
457 perhaps in the source amplitude specification, the latter only including spontaneous ad-
458 justment. “Classical” geostrophic adjustment of the kind arising after short gravity waves
459 breaking (secondary emission) could also be considered (Vadas et al., 2003; Lott, 2003).
460 In any case, the choice of including sources at all model levels stays a valid option. Sec-
461 ondary emission, for instance, generates waves at altitudes where primary GWs break,
462 and this usually takes place well in the middle atmosphere.

463 Current efforts of GW parameterization development are generally focused on adding
464 complexity in the way parameterizations treat wave propagation and dissipation (e.g.,
465 Kim et al., 2020; Plougonven et al., 2020, and references therein). Our results demon-
466 strate that modest changes in source-specifications guided by GW observations can have
467 desirable effects in both the realism of the energy spectra and the simulated middle at-

468 atmospheric circulation in a climate model. These changes are much less computationally
 469 demanding than the development of schemes allowing lateral propagation (e.g., Bölöni
 470 et al., 2016). Since an argument for including lateral propagation is that columnar prop-
 471 agation hinders GWs to propagate to specific regions where they are needed, our approach
 472 provides a stopgap to represent the desirable waves.

473 **Acknowledgments**

474 This work was supported by the Laboratoire de Recherche Conventienn Yves Rocard,
 475 a collaborative unit between CEA and Ecole Normale Supérieure. BR acknowledges fund-
 476 ing from the European project ARISE 2 (Horizon 2020, GAN653980), FL from VESRI
 477 Schmidt Future project "DataWave", and AC from the Santander-UCM grant StratWars
 478 (PR87/19-22679).

479 **References**

- 480 Alexander, M. J. (2015). Global and seasonal variations in three-dimensional gravity
 481 wave momentum flux from satellite limb-sounding temperatures. *Geophys. Res.*
 482 *Lett.*, *42*(16), 6860–6867. doi: 10.1002/2015GL065234
- 483 Alexander, M. J., & Dunkerton, T. J. (1999). A Spectral Parameterization of Mean-
 484 Flow Forcing due to Breaking Gravity Waves. *J. Atmos. Sci.*, *56*(24), 4167–
 485 4182. doi: 10.1175/1520-0469(1999)056<4167:ASPOMF>2.0.CO;2
- 486 Alexander, M. J., Geller, M., McLandress, C., Polavarapu, S., Preusse, P., Sassi, F.,
 487 ... Watanabe, S. (2010). Recent developments in gravity-wave effects in cli-
 488 mate models and the global distribution of gravity-wave momentum flux from
 489 observations and models. *Q. J. R. Meteorol. Soc.*, *136*, 1103-1124.
- 490 Alexander, M. J., Liu, C. C., Bacmeister, J., Bramberger, M., Hertzog, A., &
 491 Richter, J. H. (2021). Observational validation of parameterized gravity 2
 492 waves from tropical convection in the whole 3 atmosphere community climate
 493 model (waccm). *J. Geophys. Res.*, Submitted.
- 494 Amemiya, A., & Sato, K. (2016). A new gravity wave parameterization including
 495 three-dimensional propagation. *Journal of the Meteorological Society of Japan.*
 496 *Ser. II*, *94*(3), 237-256. doi: 10.2151/jmsj.2016-013
- 497 Baumgarten, G., Fiedler, J., Hildebrand, J., & Luebken, F.-J. (2016). Inertia
 498 gravity wave in the stratosphere and mesosphere observed by doppler wind

- 499 and temperature lidar. *Geophys. Res. Lett.*, *42*(24), 10929-10936. doi:
500 10.1002/2015GL066991
- 501 Bellenger, H., Wilson, R., Davison, J. L., Duvel, J. P., Xu, W., Lott, F., & Kat-
502 sumata, M. (2017). Tropospheric turbulence over the tropical open ocean:
503 Role of gravity waves. *Journal of the Atmospheric Sciences*, *74*(4), 1249 -
504 1271. doi: 10.1175/JAS-D-16-0135.1
- 505 Berner, J., Achatz, U., Batt, L., Bengtsson, L., de La Cámara, H. M., A. Chris-
506 tensen, Colangeli, M., ... Yano, J.-I. (2017). Stochastic parameterization
507 toward a new view of weather and climate models. *Bull. Amer. Meteor. Soc.*,
508 *98*(3), 565-587. doi: 10.1175/BAMS-D-15-00268.1
- 509 Bölöni, G., Ribstein, B., Muraschko, J., Sgoff, C., Wei, J., & Achatz, U. (2016,
510 dec). The Interaction between Atmospheric Gravity Waves and Large-Scale
511 Flows: An Efficient Description beyond the Nonacceleration Paradigm.
512 *Journal of the Atmospheric Sciences*, *73*(12), 4833-4852. Retrieved from
513 <http://journals.ametsoc.org/doi/10.1175/JAS-D-16-0069.1> doi:
514 10.1175/JAS-D-16-0069.1
- 515 Brethouwer, P., G. Billant, Lindborg, E., & Chomaz, J.-M. (2007). Scaling analysis
516 and simulation of strongly stratified turbulent flows. *J. Fluid Mech.*, *585*, 343-
517 368. doi: 10.1017/S0022112007006854
- 518 Broutman, D., & Young, W. (1986). On the interaction of small-scale oceanic inter-
519 nal waves with near-inertial waves. *J. Fluid. Mech.*, *166*, 341-358.
- 520 Bushell, A. C., Butchart, N., Derbyshire, S. H., Jackson, D. R., Shutts, G. J.,
521 Vosper, S. B., & Webster, S. (2015). Parameterized gravity wave momen-
522 tum fluxes from sources related to convection and large-scale precipitation
523 processes in a global atmosphere model. *Journal of the Atmospheric Sciences*,
524 *72*(11), 4349-4371.
- 525 Cot, C. (2001). Equatorial mesoscale wind and temperature fluctuations in the lower
526 atmosphere. *J. Geophys. Res.: Atmospheres*, *106*(D2), 1523-1532.
- 527 de la Cámara, A., & Lott, F. (2015). A parameterization of gravity waves emit-
528 ted by fronts and jets. *Geophys. Res. Lett.*, *42*(6), 2071-2078. doi: 10.1002/
529 2015GL063298
- 530 de la Cámara, A., Lott, F., & Abalos, M. (2016). Climatology of the middle at-
531 mosphere in lmdz: Impact of source-related parameterizations of gravity wave

- 532 drag. *J. Adv. Model. Earth Syst.*, *8*(4), 1507-1525.
- 533 de la Cámara, A., Lott, F., & Hertzog, A. (2014). Intermittency in a stochastic
534 parameterization of nonorographic gravity waves. *J. Geophys. Res.: Atmo-*
535 *spheres*, *119*(21), 11905-11919. doi: 10.1002/2014JD022002
- 536 de la Cámara, A., Lott, F., Jewtoukoff, V., Plougonven, R., & Hertzog, A. (2016).
537 On the gravity wave forcing during the southern stratospheric final warming in
538 lmdz. *J. Atmos. Sci.*, *73*(8), 3213-3226.
- 539 Dewan, E. M., & Good, R. E. (1986). Saturation and the universal spectrum for
540 vertical profiles of horizontal scalar winds in the atmosphere. *J. Geophys. Res.*,
541 *91*, 2742-2748.
- 542 Dörnbrack, A., Gisinger, S., Kaifler, N., Portele, T. C., Bramberger, M., Rapp, M.,
543 ... Jelić, D. (2018). Gravity waves excited during a minor sudden strato-
544 spheric warming. *Atmospheric Chemistry and Physics*, *18*(17), 12915–12931.
545 Retrieved from <https://acp.copernicus.org/articles/18/12915/2018/>
546 doi: 10.5194/acp-18-12915-2018
- 547 Eckermann, S. D. (2011). Explicitly Stochastic Parameterization of Nonorographic
548 Gravity Wave Drag. *J. Atmos. Sci.*, *68*, 1749–1765. doi: 10.1175/2011JAS3684
549 .1
- 550 Gelaro, R., McCarty, W., Suárez, M. J., Todling, R., Molod, A., Takacs, L., ...
551 Zhao, B. (2017, jul). The Modern-Era Retrospective Analysis for Research
552 and Applications, Version 2 (MERRA-2). *Journal of Climate*, *30*(14),
553 5419–5454. Retrieved from [http://journals.ametsoc.org/doi/10.1175/](http://journals.ametsoc.org/doi/10.1175/JCLI-D-16-0758.1)
554 [JCLI-D-16-0758.1](http://journals.ametsoc.org/doi/10.1175/JCLI-D-16-0758.1) doi: 10.1175/JCLI-D-16-0758.1
- 555 Gelinas, L. J., Walterscheid, R. L., Mechoso, C. R., & Schubert, G. (2012). Obser-
556 vations of an inertial peak in the intrinsic wind spectrum shifted by rotation in
557 the antarctic vortex. *Journal of the Atmospheric Sciences*, *69*(12), 3800–3811.
558 doi: 10.1175/JAS-D-11-0305.1
- 559 Hertzog, A., Alexander, M. J., & Plougonven, R. (2012). On the Intermittency
560 of Gravity Wave Momentum Flux in the Stratosphere. *Journal of the Atmo-*
561 *spheric Sciences*(11), 3433–3448. doi: 10.1175/JAS-D-12-09.1
- 562 Hertzog, A., Boccara, G., Vincent, R., F. Vial, F., & Cocquerez, P. (2008). Estima-
563 tion of gravity wave momentum flux and phase speeds from quasilagrangian
564 stratospheric balloon flights. part ii: Results from the vorcore campaign in

- 565 antarctica. *Journal of the Atmospheric Sciences*(65), 3056–3070.
- 566 Hines, C. (1996). Nonlinearity of gravity wave saturated spectra in the middle atmo-
567 sphere. *Geophys. Res. Lett.*, 23(23).
- 568 Hines, C. O. (1997). Doppler-spread parameterization of gravity-wave momentum
569 deposition in the middle atmosphere. part 2: Broad and quasi monochromatic
570 spectra, and implementation. *J. Atmos. Solar Terr. Phys.*, 59(4), 387-400. doi:
571 10.1016/S1364-6826(96)00080-6
- 572 Hourdin, F., Foujols, M., Codron, F., Guemas, V., Dufresne, J.-L., Bony, S., ...
573 Bopp, L. (2013). Impact of the lmdz atmospheric grid configuration on the
574 climate and sensitivity of the ipsl-cm5a coupled model. *Climate Dynamics*,
575 40(9-10), 2167-2192. doi: 10.1007/s00382-012-1411-3
- 576 Hourdin, F., Rio, C., Grandpeix, J.-Y., Madeleine, J.-B., Cheruy, F., Rochetin,
577 N., ... Ghattas, J. (2020). Lmdz6a: The atmospheric component of
578 the ipsl climate model with improved and better tuned physics. *Jour-
579 nal of Advances in Modeling Earth Systems*, 12(7), e2019MS001892. doi:
580 https://doi.org/10.1029/2019MS001892
- 581 Khaykin, S. M., Hauchecorne, A., Mz e, N., & Keckhut, P. (2015). Seasonal vari-
582 ation of gravity wave activity at midlatitudes from 7years of cosmic gps and
583 rayleigh lidar temperature observations. *Geophysical Research Letters*, 42(4),
584 1251-1258. doi: 10.1002/2014GL062891
- 585 Kim, Y.-H., B ol oni, G., Borchert, S., Chun, H.-Y., & Achatz, U. (2020). Towards
586 transient subgrid-scale gravity wave representation in atmospheric models.
587 Part II: Wave intermittency simulated with convective sources. *Journal of the
588 Atmospheric Sciences*, 1–49. doi: 10.1175/JAS-D-20-0066.1
- 589 Lilly, D. K. (1983). Stratified turbulence and the mesoscale variability of the atmo-
590 sphere. *J. Atmos. Sci.*, 40(3), 749-761. doi: 10.1175/1520-0469(1983)040<0749:
591 STATMV>2.0.CO;2
- 592 Lindborg, E. (2006). The energy cascade in a strongly stratified fluid. *J. Fluid
593 Mech.*, 550, 207-242. doi: 10.1017/S0022112005008128
- 594 Lindzen, R. S., & Schoeberl, M. R. (1982). A note on the limits of rossby wave
595 amplitudes. *J. Atmos. Sci.*, 39(5), 1171-1174. doi: 10.1175/1520-0469(1982)
596 039<1171:ANOTLO>2.0.CO;2
- 597 Lott, F. (2003). Large-scale flow response to short gravity waves breaking in a rotat-

- 598 ing shear flow. *Journal of the atmospheric sciences*, 60(14), 1691–1704.
- 599 Lott, F., & Guez, L. (2013). A stochastic parameterization of the gravity waves due
600 to convection and its impact on the equatorial stratosphere. *J. Geophys. Res.*,
601 118(16), 8897-8909. doi: 10.1002/jgrd.50705
- 602 Lott, F., Guez, L., & Maury, P. (2012). A stochastic parameterization of non-
603 orographic gravity waves: Formalism and impact on the equatorial strato-
604 sphere. *Geophys. Res. Lett.*, 39(6), L06807. doi: 10.1029/2012GL051001
- 605 Lott, F., & Miller, M. J. (1997, jan). A new subgrid-scale orographic drag
606 parametrization: Its formulation and testing. *Quarterly Journal of*
607 *the Royal Meteorological Society*, 123(537), 101–127. Retrieved from
608 [http://www.ingentaselect.com/rpsv/cgi-bin/cgi?ini=xref{\&}body=](http://www.ingentaselect.com/rpsv/cgi-bin/cgi?ini=xref{\&}body=linker{\&}reqdoi=10.1256/smsqj.53703)
609 [linker{\&}reqdoi=10.1256/smsqj.53703](http://www.ingentaselect.com/rpsv/cgi-bin/cgi?ini=xref{\&}body=linker{\&}reqdoi=10.1256/smsqj.53703) doi: 10.1256/smsqj.53703
- 610 Lott, F., Millet, C., & Vanneste, J. (2015). Inertia-gravity waves in inertially stable
611 and unstable shear flows. *J. Fluid Mech.*, 775, 223-240.
- 612 Lott, F., Plougonven, R., & Vanneste, J. (2012). Gravity waves generated by sheared
613 three-dimensional potential vorticity anomalies. *Journal of the Atmospheric*
614 *Sciences*, 69(7), 2134-2151. doi: 10.1175/JAS-D-11-0296.1
- 615 Love, P. T., & Murphy, D. J. (2016). Gravity wavemomentum flux in themeso-
616 spheremeasured by vhf radar at davis, antarctica. *J. Geophys. Res.: Atmo-*
617 *spheres*, 121(21), 12723-12736. doi: 10.1002/2016JD025627
- 618 Manzini, E., McFarlane, N. A., & McLandress, C. (1997). Impact of the doppler
619 spread parameterization on the simulation of the middle atmosphere circula-
620 tion using the ma/echam4 general circulation model. *Journal of Geophysical*
621 *Research: Atmospheres*, 102(D22), 25751-25762. doi: 10.1029/97JD01096
- 622 Métais, O., Bartello, P., Garnier, E., Riley, J. J., & Lesieur, M. (1996). Inverse
623 cascade in stably stratified rotating turbulence. *Dyn. Atmos. Oceans*, 23(1-4),
624 193-203.
- 625 Muraschko, J., Fruman, M., Achatz, U., Hickel, S., & Toledo, Y. (2015). On the
626 application of wentzel–kramer–brillouin theory for the simulation of the weakly
627 nonlinear dynamics of gravity waves. *Quarterly Journal of the Royal Meteorolo-*
628 *gical Society*, 141(688), 676–697.
- 629 Palmer, T. N., Shutts, G. J., & Swinbank, R. (1986). Alleviation of a system-
630 atic westerly bias in general circulation and numerical weather prediction

- 631 models through an orographic gravity wave drag parametrization. *Quar-*
 632 *terly Journal of the Royal Meteorological Society*, 112(474), 1001-1039. doi:
 633 10.1002/qj.49711247406
- 634 Plougonven, R., de la Cámara, A., Hertzog, A., & Lott, F. (2020). How does knowl-
 635 edge of atmospheric gravity waves guide their parameterizations? *Q. J. Roy.*
 636 *Meteor. Soc.*. doi: 10.1002/qj.3732
- 637 Plougonven, R., Jewtoukoff, V., de la Cámara, A., Lott, F., & Hertzog, A. (2017).
 638 On the relation between gravity waves and wind speed in the lower strato-
 639 sphere over the southern ocean. *J. Atmos. Sci.*, 74(4), 1075-1093. doi:
 640 10.1175/JAS-D-16-0096.1
- 641 Plougonven, R., & Zhang, F. (2014, mar). Internal gravity waves from atmospheric
 642 jets and fronts. *Rev. Geophys.*, 52(1), 33-76. Retrieved from [http://doi](http://doi.wiley.com/10.1002/2012RG000419)
 643 [.wiley.com/10.1002/2012RG000419](http://doi.wiley.com/10.1002/2012RG000419) doi: 10.1002/2012RG000419
- 644 Polichtchouk, I., & Scott, R. K. (2020). Spontaneous inertia-gravity wave emission
 645 from a nonlinear critical layer in the stratosphere. *Quarterly Journal of the*
 646 *Royal Meteorological Society*, 146(728), 1516-1528.
- 647 Reichert, R., Kaifler, B., Kaifler, N., Rapp, M., Pautet, P.-D., Taylor, M. J.,
 648 ... Kivi, R. (2019). Retrieval of intrinsic mesospheric gravity wave
 649 parameters using lidar and airglow temperature and meteor radar wind
 650 data. *Atmospheric Measurement Techniques*, 12(11), 5997-6015. Re-
 651 trieved from <https://www.atmos-meas-tech.net/12/5997/2019/> doi:
 652 10.5194/amt-12-5997-2019
- 653 Ribstein, B., & Achatz, U. (2016). The interaction between gravity waves and solar
 654 tides in a linear tidal model with a 4-d ray-tracing gravity-wave parameteriza-
 655 tion. *J. Geophys. Res.: Space Physics*, 121(9).
- 656 Sato, K., & Yoshiki, M. (2008). Gravity wave generation around the polar vortex in
 657 the stratosphere revealed by 3-hourly radiosonde observations at syowa station.
 658 *Journal of the Atmospheric Sciences*, 65(12), 3719-3735.
- 659 Shibuya, R., & Sato, K. (2019, 03). A study of the dynamical characteristics of
 660 inertiagravity waves in the antarctic mesosphere combining the pansy radar
 661 and a non-hydrostatic general circulation model. *Atmospheric Chemistry and*
 662 *Physics*, 19, 3395-3415. doi: 10.5194/acp-19-3395-2019
- 663 Smith, A. K., Garcia, R. R., Moss, A. C., & Mitchell, N. J. (2017, aug). The

- 664 Semiannual Oscillation of the Tropical Zonal Wind in the Middle At-
 665 mosphere Derived from Satellite Geopotential Height Retrievals. *Jour-*
 666 *nal of the Atmospheric Sciences*, 74(8), 2413–2425. Retrieved from
 667 <http://journals.ametsoc.org/doi/10.1175/JAS-D-17-0067.1> doi:
 668 10.1175/JAS-D-17-0067.1
- 669 Souprayen, C., Vanneste, J., Hertzog, A., & Hauchecorne, A. (2001). Atmospheric
 670 gravity-wave spectra: A stochastic approach. *J. Geophys. Res.*, 106, 24,071-
 671 24,086.
- 672 Tsuda, T., Murayama, Y., Wiriyosumarto, H., Harijono, S. W. B., & Kato, S. (1994).
 673 Radiosonde observations of equatorial atmosphere dynamics over indonesia 2.
 674 characteristics of gravity waves. *J. Geophys. Res.*, 99(D5), 10507-10516.
- 675 Vadas, S. L., Fritts, D. C., & Alexander, M. J. (2003). Mechanism for the gener-
 676 ation of secondary waves in wave breaking regions. *Journal of the atmospheric*
 677 *sciences*, 60(1), 194–214.
- 678 Vincent, R. A., & Alexander, M. J. (2020). Balloon-borne observations of short
 679 vertical wavelength gravity waves and interaction with qbo winds. *Journal of*
 680 *Geophysical Research: Atmospheres*, 125(15), e2020JD032779. doi: [https://doi](https://doi.org/10.1029/2020JD032779)
 681 [.org/10.1029/2020JD032779](https://doi.org/10.1029/2020JD032779)
- 682 Warner, C. D., & McIntyre, M. E. (1996). On the propagation and dissipation
 683 of gravity wave spectra through a realistic middle atmosphere. *J. Atmos. Sci.*,
 684 53(22), 3213-3235. doi: 10.1175/1520-0469(1996)053<3213:OTPADO>2.0.CO;
 685 2
- 686 Wright, C. J., Osprey, S. M., & Gille, J. C. (2013). Global observations of gravity
 687 wave intermittency and its impact on the observed momentum flux mor-
 688 phology. *J. Geophys. Res. Atmos.*, 118(19), 10,980–10,993. Retrieved from
 689 <http://doi.wiley.com/10.1002/jgrd.50869> doi: 10.1002/jgrd.50869
- 690 Zhao, J., Chu, X., Chen, C., Lu, X., Fong, W., Yu, Z., ... Dörnbrack, A. (2017). Li-
 691 dar observations of stratospheric gravity waves from 2011 to 2015 at mcmurdo
 692 (77.84°s, 166.69°e), antarctica: 1. vertical wavelengths, periods, and frequency
 693 and vertical wave number spectra. *J. Geophys. Res.: Atmospheres*, 122(10),
 694 5041-5062. doi: 10.1002/2016JD026368

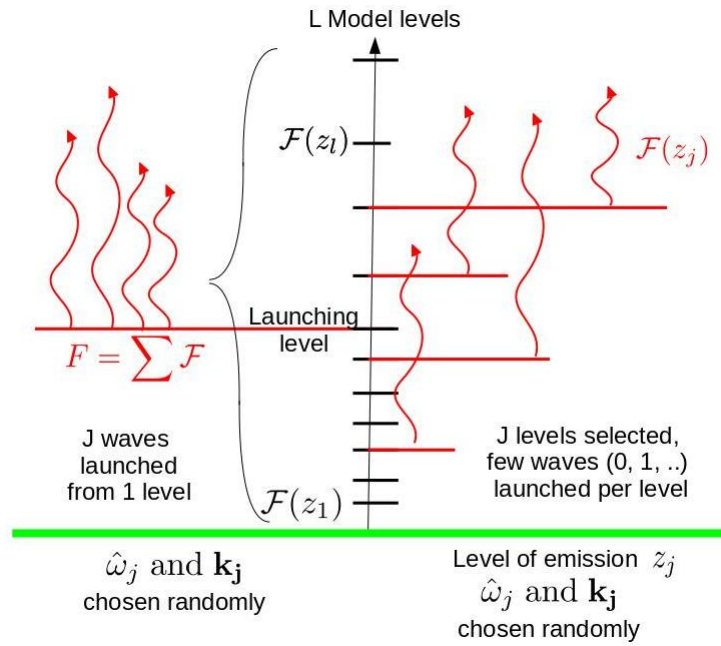


Figure 1. Schematic representation of the scheme used in (de la Cámara & Lott, 2015) (left) and of its modification to include waves emitted from all model levels (right).

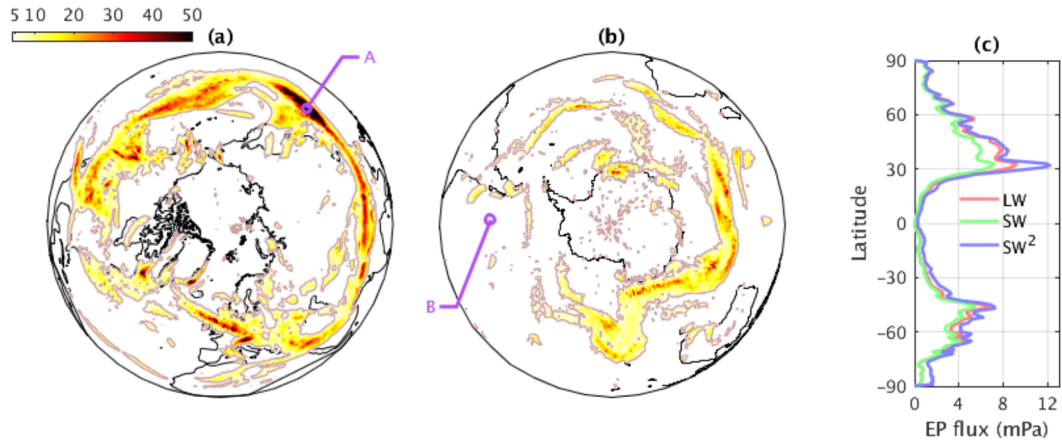


Figure 2. (a,b) Horizontal distribution of the total EP flux (mPa) at pressure level 500 hPa in the SW-ML setup. The geographical locations A and B are the locations where the energy spectra are constructed as shown in Figure 3. (c) Zonal mean EP flux at 500 hPa for the three GWs configurations.

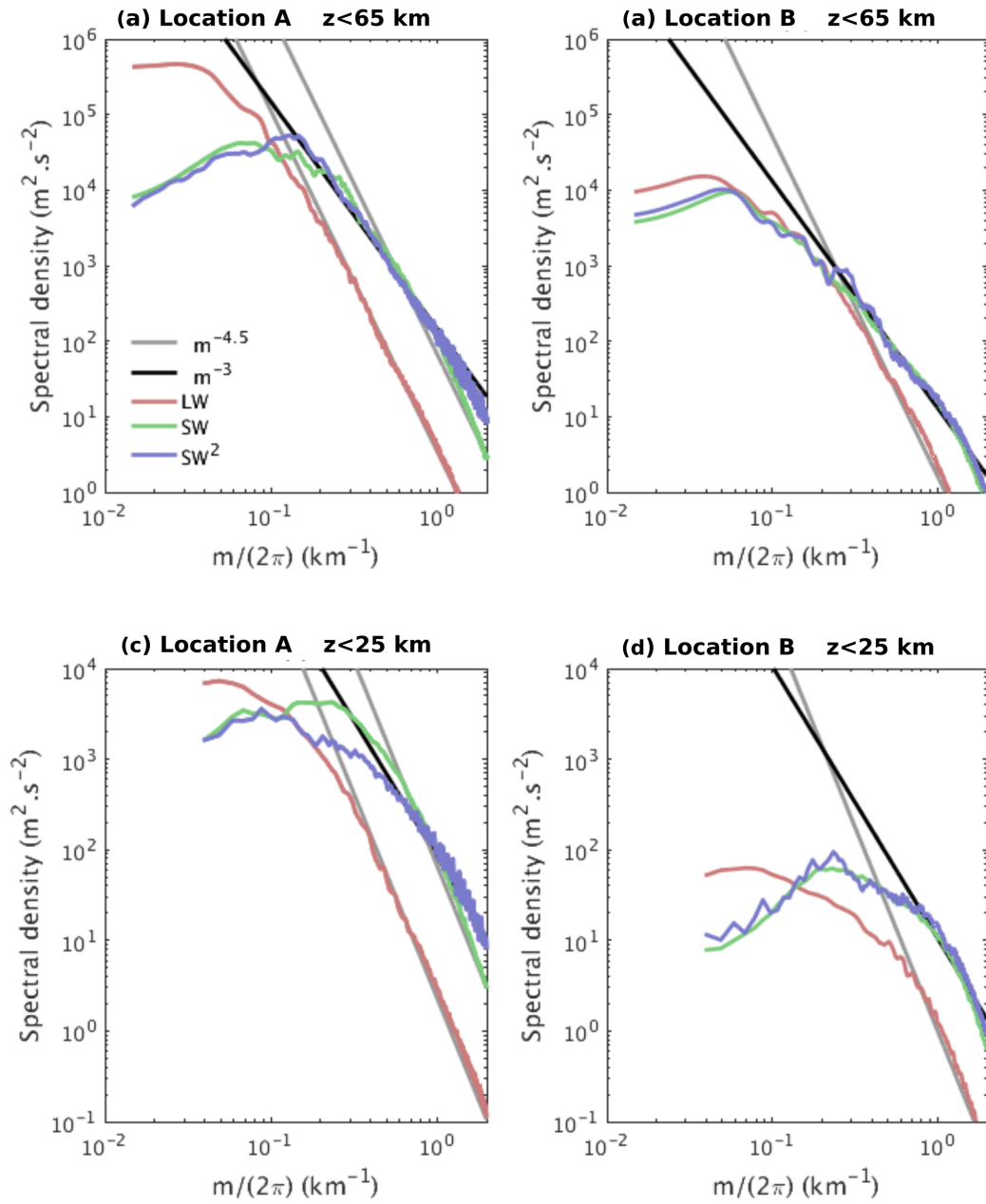


Figure 3. Zonal wind spectra from realizations of the GWs fields obtained using parameterizations LW, SW-1L and SW-ML, respectively, for locations A (a,c) and B (b,d) (see figure 2) and altitude ranges 0-65 km (a,b) and 0-25 km (c,d).

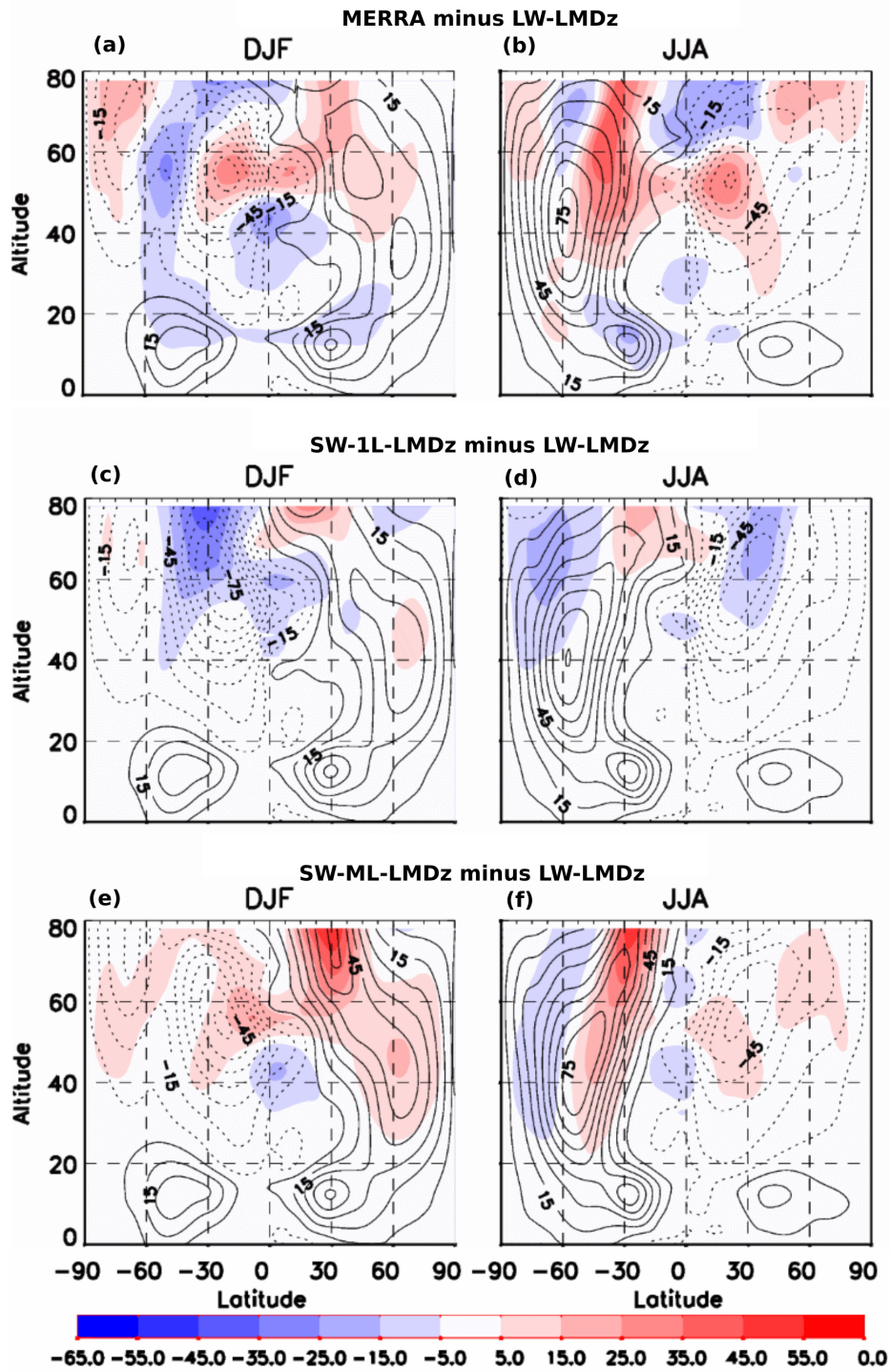


Figure 4. Cross-sections of zonal mean zonal wind from the three experiments (black contours, interval: $10\text{m}\cdot\text{s}^{-1}$): a) DJF LW-LMDz, b) JJA LW-LMDz, c) DJF SW-1L-LMDz, d) JJA SW-1L-LMDz, e) DJF SW-ML-LMDz, and f) JJA SW-ML-LMDz. The color shading corresponds to the differences between LW-LMDz minus MERRA in a) and b), SW-1L-LMDz minus LW-LMDz in c), and d), and SW-ML-LMDz minus LW-LMDz in e) and f). Units are in $\text{m}\cdot\text{s}^{-1}$

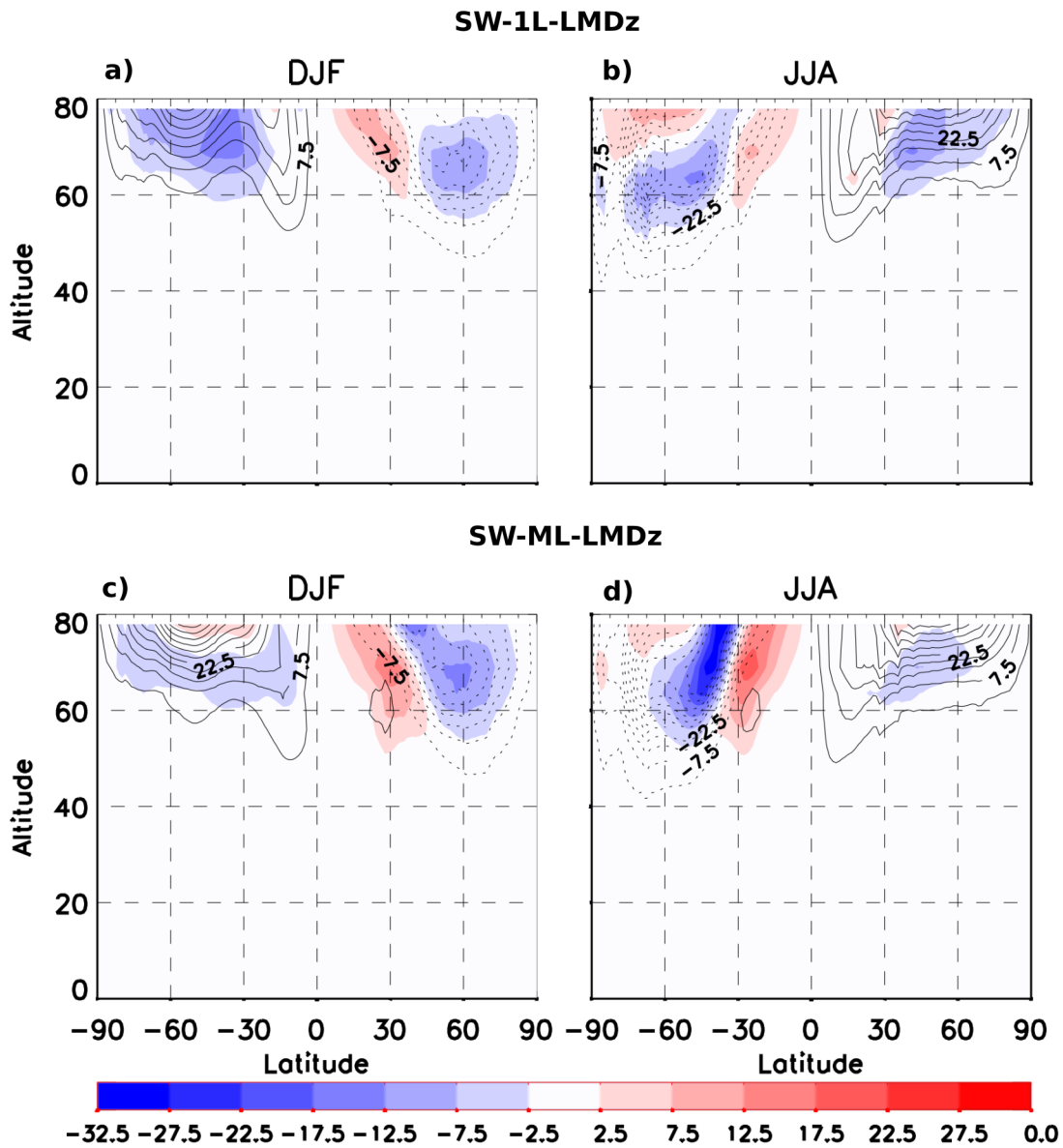


Figure 5. Cross-sections of zonal mean GW drag (black contours, interval: $5\text{m}\cdot\text{s}^{-2}$), for a) SW-1M-LMDz and DJF, b) SW-1ML-LMDz and JJA, c) DJF SW-1L-LMDz and DJF, and d) SW-1L-LMDz and JJA. The color shading represents the difference with respect to LW-LMDz.

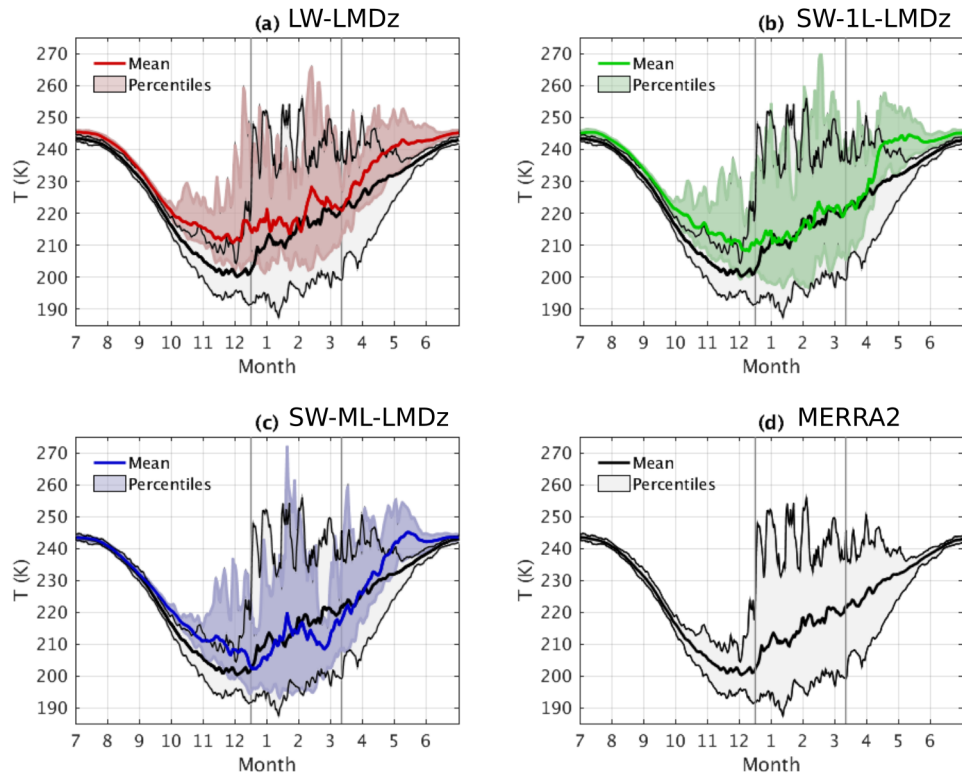


Figure 6. Annual cycle of the simulated mean temperature over a period of 15 years and associated 5th and 95th percentiles at 10 hPa and latitude 80° N. (a) LW-LMDz, (b) SW-LMDz, and (c) SW-ML-LMDz. The Observed 1996 - 2010 mean temperatures from MERRA2 (d) are superimposed to simulated results.